

Composition Tunability and (111)-Dominant Facets of Ultrathin Platinum–Gold Alloy Nanowires toward Enhanced Electrocatalysis

Fangfang Chang,^{†,‡} Shiyao Shan,[†] Valeri Petkov,[§] Zakiya Skeete,[†] Aolin Lu,[†] Jonathan Ravid,[†] Jinfang Wu,[†] Jin Luo,[†] Gang Yu,[‡] Yang Ren,^{||} and Chuan-Jian Zhong^{*,†}

[†]Department of Chemistry, State University of New York at Binghamton, Binghamton, New York 13902, United States

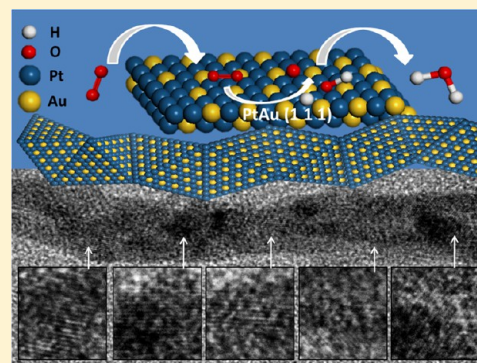
[‡]College of Chemistry and Chemical Engineering, Hunan University, Changsha 410082, China

[§]Department of Physics, Central Michigan University, Mt. Pleasant, Michigan 48859, United States

^{||}X-ray Science Division, Advanced Photon Source, Argonne National Laboratory, Argonne, Illinois 60439, United States

S Supporting Information

ABSTRACT: The ability for tuning not only the composition but also the type of surface facets of alloyed nanomaterials is important for the design of catalysts with enhanced activity and stability through optimizing both ensemble and ligand effects. Herein we report the first example of ultrathin platinum–gold alloy nanowires (PtAu NWs) featuring composition-tunable and (111) facet-dominant surface characteristics, and the electrocatalytic enhancement for the oxygen reduction reaction (ORR). PtAu NWs of different bimetallic compositions synthesized by a single-phase and surfactant-free method are shown to display an alloyed, parallel-bundled structure in which the individual nanowires exhibit Boerdijk–Coxeter helix type morphology predominant in (111) facets. Results have revealed intriguing catalytic correlation with the binary composition, exhibiting an activity maximum at a Pt: Au ratio of $\sim 3:1$. As revealed by high-energy synchrotron X-ray diffraction and atomic pair distribution function analysis, NWs of this ratio exhibit a clear shrinkage in interatomic bonding distances. In comparison with PtAu nanoparticles of a similar composition and degree of shrinking of atomic-pair distances, the PtAu NWs display a remarkably higher electrocatalytic activity and stability. The outperformance of NWs over nanoparticles is attributed to the predominant (111)-type facets on the surface balancing the contribution of ensemble and ligand effects, in addition to the composition synergy due to optimal adsorption energies for molecular and atomic oxygen species on the surface as supported by DFT computation of models of the catalysts. The findings open up a new pathway to the design and engineering of alloy nanocatalysts with enhanced activity and durability.



1. INTRODUCTION

The increasing demand for efficient energy conversion and low environmental impact has raised a great deal of interest in the development of proton-exchange membrane fuel cells (PEMFCs) for commercial applications.^{1–3} The ultimate commercialization of PEMFCs, however, must address a key challenge for the sluggish reaction kinetics at the cathode, i.e., oxygen reduction reaction (ORR), which requires not only highly active but also stable and low-cost catalysts.^{4–7} Platinum is considered to be the most active cathode electrocatalyst for the ORR but is not stable and is too expensive to be sustainable because of limited global supply of platinum. Pt-based bimetallic catalysts^{8,9} and catalysts formed by alloying transition metals into Pt have been an important focus in the design of catalysts for the ORR.^{9–13} Recent experimental results indicate that one-dimensional (1D) Pt-based nanostructures which are characterized by their uniquely anisotropic nature¹⁴ may be advantageous compared to zero-dimensional (0D) Pt nanoparticles, as the 1D suffers less from dissolution and Ostwald ripening/aggregation.¹⁵ The activity enhancements are generally

attributed to several factors,¹⁶ including 1D shape favoring reaction mass transport with reduced activation polarization, extended surface structure weakening interactions with oxygen containing species (i.e., OH_{ad}) with improved ORR kinetics,^{17,18} and increased surface area to volume in comparison with nanoparticle counterparts.¹⁹ There are several studies reporting the enhancement of the electrocatalytic activity of the ORR over 1D nanostructures derived from noble metals.^{16,20} For example, 1D ultrathin (<2 nm) platinum nanowires²¹ synthesized by a surfactantless technique exhibited a specific activity (1.45 mA/cm²) which is a 7-fold increase in comparison with that of commercial Pt/C. These as-prepared ultrathin nanowires feature low-energy crystalline facets and a <111> growth direction. Pd_{1–x}Au_x and Pd_{1–x}Pt_x nanowires synthesized by the template-based technique²² also showed significantly enhanced activity (2–4 fold) toward oxygen reduction in comparison with commercial Pt. Recently, Cu@CuPt core@shell nanowires synthesized using

Received: May 19, 2016

Published: September 12, 2016

Cu nanowires as a template in organic solvent medium were shown to exhibit 3-fold increase in mass activity in comparison with commercial Pt/C catalysts.²³ Other types of platinum-based nanostructures such as nanocages with surfaces being enriched with both {111} facets and twin boundaries have also been shown to exhibit significant enhancement in electrocatalytic activity toward the ORR.^{24,25}

There has been a great deal of interest in exploring gold as part of the catalysts, which stems largely from its inertness in the bulk state and the unprecedented catalytic properties when gold materials are reduced to the nanoscale dimension.^{26,27} In view of nanogold's unique catalytic properties^{28,29} and the high stability,³⁰ bimetallic PtAu nanoparticles serve as an ideal model system for Pt alloys in assessing the synergistic catalytic properties. For example, in alkaline medium the addition of Au into Pt catalysts was found to provide adsorption sites for OH species but to reduce the strength of Pt–OH formation.^{31,32} On the other hand, the addition of Au to Pt would theoretically increase the lattice distance of Pt. Furthermore, Au has an electronegativity higher than that of Pt which could increase the charge transfer from Pt atoms to Au atoms. To address how these structural characteristics correlate with the catalytic properties, 1D NWs of PtAu provide an ideal platform for investigation, considering that 0D PtAu nanoparticles have been extensively studied, including our own work,^{13,33–38} and there are also reports on 1D PtAu NWs in terms of synthesis,^{39–41} morphologies,^{42,43} and properties.^{43–47} While there are reports on Au/Pt and Au/Pt₃Ni nanostructures derived by growing Pt and Pt₃Ni alloy nanodendrites on Au nanowires and their ORR activity and durability,⁴⁸ little has been reported on the 1D PtAu NWs in terms of the correlation between the composition- and facet-tuned structures and the electrocatalytic properties. Herein we report the first example of PtAu nanowires featuring an ultrathin Boerdijk–Coxeter helix type of structure with (111) facet-dominant surfaces, and the correlation between such NW structure/composition and the electrocatalytic activity and stability properties. Important insights into this correlation are gained by characterization using synchrotron high-energy X-ray diffraction (HE-XRD) which is coupled to atomic pair distribution function (PDF) analysis.

2. EXPERIMENTAL SECTION

2.1. Chemicals. Hydrogen tetrachloroaurate(III) hydrate (HAuCl₄, 99%) and hydrogen hexachloroplatinate(IV) (H₂PtCl₆·6H₂O, 99.995%) were purchased from Alfa Aesar. Potassium hydroxide (KOH, 85+%), ethylene glycol anhydrous (EG, 99.8%), *N,N*-dimethylformamide (DMF, 99.8%), and Nafion (5 wt %) were obtained from Aldrich. Hexane, ethanol, and potassium chloride were obtained from Fisher. Vulcan XC-72 carbon was obtained from Cabot. A Millipore Milli-Q water system was used for purification of deionized water (DI). Pt/C catalyst (from E-tek, 20 wt % metal loading) was purchased from Strem Chemicals. Gases such N₂, O₂, and H₂ were obtained from Airgas.

2.2. Nanowire Synthesis and Catalyst Preparation. Pt_{*n*}Au_{100–*n*} nanowires were synthesized by a modified hydrothermal method.^{49,50} Briefly, 1.0 g of KOH was added to a solution containing 6 mL of EG and 9 mL of DMF. After potassium hydroxide was completely dissolved, 2.4 mL of hydrogen hexachloroplatinate(IV) and 1.0 mL of hydrogen tetrachloroaurate(III) hydrate were added to the mixture solution. The composition of the Pt_{*n*}Au_{100–*n*} nanowires was controlled by the feeding molar ratio. After magnetic stirring overnight, the solution was transferred into an autoclave with a Teflon interior (20 mL size). The autoclave was heated and maintained at 180 °C for 8 h before cooling to room temperature. The resulting PtAu NWs were then precipitated by centrifugation and redispersed in DI water for future use. The preparation of supported nanowire catalysts then involved assembly of

the nanowires on a support and subsequent thermochemical processing for activation of the catalysts. Briefly, the carbon powder was dispersed in DI water by ultrasonication for 30 min. A controlled amount of PtAu nanowires was mixed with the well-dispersed carbon suspension under extensive stirring for 30 min. A 150 mL amount of ethanol was added to the solution to remove amines and to deposit the carbon-supported PtAu nanowires, PtAu NWs/C. The PtAu NWs/C were collected by centrifugation and then dried in an oven at 70 °C overnight. The mass loading of catalysts was determined by thermogravimetric analysis (TGA) using PerkinElmer Pyris 1-TGA. The weight loading of most catalysts reported here was within 14–28 wt % (e.g., 28% for Pt₁₆Au₈₄/C and Pt₄₉Au₅₁/C, 15% for Pt/C, 16% for Pt₉₀Au₁₀/C, and 14% for Pt₇₆Au₂₄/C).

PtAu nanoparticles were also prepared similarly except for increasing platinum and gold concentrations and decreasing the reaction time. Briefly, to prepare Pt₇₆Au₂₄ nanoparticles, 1.6 g of KOH was added to a solution containing 6 mL of EG and 9 mL of DMF. A 79.0 mg amount of H₂PtCl₆·6H₂O and 19.5 mg of HAuCl₄·3H₂O were added to the above solution mixture after the KOH was completely dissolved. After magnetic stirring overnight, the solution was transferred into the autoclave. After heating at 180 °C for 1 h and cooling to room temperature, the resulting PtAu NPs (Pt₇₆Au₂₄) were precipitated by washing and centrifugation. The Pt₇₆Au₂₄ NPs were supported on carbon materials and dried in oven overnight. The weight loading of Pt₇₆Au₂₄NPs/C was determined to be 19%.

2.3. Characterization of Catalysts. Inductively Coupled Plasma–Optical Emission Spectroscopy (ICP-OES). The chemical composition of PtAu NWs was analyzed using ICP-OES. A PerkinElmer 2000 DV ICP-OES instrument was used for the analysis.⁵¹ Standards were analyzed frequently as a check. If the standards were above ±5% of the initial concentration, recalibration of the instrument was then performed.

Transmission Electron Microscopy (TEM). JEOL JEM 2010F was used for the TEM measurement. An acceleration voltage of 200 kV was used. With a point-to-point resolution of 0.194 nm, high-resolution TEM images were also obtained with the instrument. In sample preparation, a DI water suspension of the nanowires was drop-casted onto a copper grid coated with carbon film, which was then followed by evaporation of the solvent under ambient conditions.

High Energy X-ray Diffraction and Atomic Pair Distribution Functions (PDFs) Derivation. The catalysts were characterized using synchrotron high-energy XRD (HE-XRD) at Advanced Photon Source (Sector-11) at Argonne National Laboratory. Data were taken using X-rays with a wavelength, λ , of 0.1080 Å (X-ray energy ~115 keV). The carbon-supported nanowire or nanoparticle catalyst sample was sealed inside a thin-wall glass capillary (1.5 mm in diameter). The measurement was performed at room temperature. Experimental HE-XRD patterns were reduced to the structure factors, $S(q)$, before Fourier transformation to atomic pair distribution functions (PDFs) $G(r)$. Note that $G(r)$ oscillates around zero, showing positive peaks at real space distances (r) at which the local atomic density exceeds the average one.

Electrocatalytic Activity Measurement. A glassy carbon (GC) disk was used as the working electrode. The geometric area of GC was 0.196 cm². It was polished with Al₂O₃ powders (0.005 μ m). The catalyst inks were prepared by suspending 5 mg of catalyst (PtAu NWs on C) in a 5 mL aqueous solution containing 2-propanol and Nafion (5%) (4.5:0.25:0.25, $v/v/v$). Each ink was ultrasonicated for at least 40 min to ensure a homogeneous solution. Ten microliters of the ink was transferred to the GC disk surface.³³ An electrochemical analyzer (Model CHI600a, CH Instruments) was used to perform cyclic voltammetry (CV) and rotating disk electrode (RDE) measurements in a three-electrode cell configuration. The electrolytic solution (0.1 M HClO₄) was deaerated with pure nitrogen gas before CV measurements. The solution was saturated with oxygen gas in the RDE measurement. A reversible hydrogen electrode (RHE) was used as reference electrode. These measurements were performed at room temperature.

Computational Modeling. Ab initio and DFT computations were performed using DMol3 program coming as a part of Materials Studio.⁵² The computations used generalized gradient approximation with the exchange correlation function.⁵³ It involved the localized double

numerical basis sets and polarization functions for the valence orbitals, and effective core potential to account for the core electrons of metallic species. Full geometry optimizations were performed for all model atomic configurations tested here so that all atoms were fully relaxed. The configurations included unsupported small PtAu clusters. The interactions between the model atomic configurations and O₂ molecule were explored. The adsorption energies for O₂ and intermediates O_{ads} on PtAu cluster were used as measures of the adsorption strength of O₂. It was calculated by $E_{\text{ads}} = -(E_{\text{O}_2\text{-metal}} - E_{\text{metal}} - E_{\text{O}_2})$, where, $E_{\text{O}_2\text{-metal}}$, E_{metal} , and E_{O_2} are total energy for the O₂-metal complex, the isolated atomic configuration, and the isolated O₂ molecule, respectively.⁵⁴

3. RESULTS AND DISCUSSION

3.1. Nanowire Morphology and Composition. *Composition.* The relationship between Pt composition in Pt_nAu_{100-n} NWs and the synthetic feeding composition is shown in Figure 1.

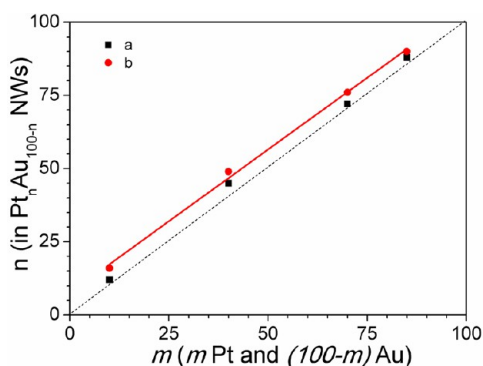


Figure 1. Plot of Pt fraction (n) in Pt_nAu_{100-n} nanowires (a) and the nanowires supported on carbon (b) (from ICP-OES analysis) vs the nominal feeding atomic fraction m (i.e., m Pt and $(100 - m)$ Au) in NW synthesis. The dashed line represents a 1:1 relationship whereas the solid one represents the linear fitting to the experimental data (slope: 0.98, $R^2 = 0.996$).

The NWs were supported on carbon. The composition of carbon-supported Pt_nAu_{100-n} (Pt₁₆Au₈₄/C, Pt₄₉Au₅₁/C, Pt₇₆Au₂₄/C, and Pt₉₀Au₁₀/C) showed very little change in comparison with the as-synthesized NWs (Pt₁₂Au₈₈, Pt₄₅Au₅₅, Pt₇₂Au₂₈, and Pt₈₈Au₁₂) (Table S1, SI), indicating a negligible effect of the nanowire-supporting process on the bimetallic composition. Data for the composition of PtAu NWs show a slope of 0.98, which is slightly lower than 1, indicating that the chemical composition of the PtAu NWs is controllable by the feeding ratio of the two metal precursors. The fact that the linear regression shows an intercept on the y-axis slightly above 0 indicates that Pt is more favored than Au in the formation of bimetallic nanowires.

Morphology. The morphology and surface structure of the Pt_nAu_{100-n} NWs are characterized by transmission electron microscopy (TEM). Figure 2 shows a typical set of TEM images for a sample of Pt₇₂Au₂₈ NWs (as synthesized). The nanowires form bundles connected into a network-like consisting of bundles of interconnected nanowires (Figure 2A,B). A close examination reveals that NWs in a bundle are ultrathin and run in parallel to each other (Figure 2C–D), with individual nanowire exhibiting an average diameter of 4.5 ± 1.0 nm. Similar morphologies have also been observed for PtAu NWs of the other compositions (e.g., Pt₁₂Au₈₈, Pt₄₅Au₅₅, Pt₈₈Au₁₂, see Figures S1–S3, SI). Note that in the case of Pt₁₂Au₈₈, the nanowire feature is less significant, indicative of the important role of Pt in the formation of the nanowires. There are two possible scenarios responsible for the formation of the network structure composed of bundles of interconnected nanowires. First, there is a propensity of forming

active defects along the nanowires which leads to coalescence upon contacting with different nanowires, forming network structures. Second, there is a strong cohesive interaction along the nanowires driven by the minimization of the total surface free energy, which is aided by hydrophobic interactions of DMFs being adsorbed on the NW surface during the synthesis of PtAu NWs. This type of morphology was not observed for PtAu NPs (see Figure S4, SI).

Figure 3 shows a representative set of high-resolution (HR) TEM images of the individual NWs, revealing domains of nanocrystal facets along the nanowire. On average, the lattice fringes from different domains are found to be spaced at a distance of about 0.231 nm, which corresponds to the distance between (111) planes in a face-centered-cubic (fcc) alloy. The average distance between the lattice fringes falls in between the distances separating (111) atomic planes in pure Au and pure Pt, indicative of an alloy-type structure. A close examination of Figure 3 reveals that the individual NWs from any given bundle features a Boerdijk–Coxeter type helix and largely terminated by (111)-type facets. Interestingly, the PtAu NWs' Boerdijk–Coxeter type helix resembles that found in Au, AuAg, and AuCu nanowires.^{55–57} Similar features characteristic of the (111) facets along the nanowires have also been observed for PtAu NWs of the other compositions (e.g., Pt₁₂Au₈₈, Pt₄₅Au₅₅, Pt₈₈Au₁₂, see Figures S1–S3, SI).

In addition to in-house XRD characterization (see Figures S5–S6, SI), the structural features of PtAu NW catalysts were further examined by HE-XRD to determine the dependence of NW structure on the composition. Figure 4A shows a set of atomic PDFs which are extracted from HE-XRD patterns for Pt_nAu_{100-n} NWs. PDFs for Pt_nAu_{100-n} NPs (Figure 4B) were studied in great detail in our previous report.⁵⁸ It is evident that the general characteristics of the PDFs are quite similar between the NWs and NPs, indicating similar, fcc-type alloy structures.

Lattice parameters extracted from fcc-type fits to the experimental PDFs data are summarized in Figure 5. The lattice parameters for bulk Pt and Au are also included for comparison. While the data are in general very close to the linear relationship, characteristic of alloying according to Vegard's law based on the lattice parameters of Au and Pt, subtle differences can be observed in terms of small deviations from the linear relationship simply based on Au and Pt lattice parameters. In particular, such deviations appear to depend on the morphology of the nanomaterials, revealing differences between NWs and NPs. For NWs, there is a lattice expansion when Pt% is less than ~60% but a small lattice shrinking when Pt% is greater than ~60%. This is in sharp contrast to NPs with which lattice shrinking is evident for all compositions. When Pt% is larger than 50–60%, both NWs and NPs exhibit similar lattice shrinking, where the extent of shrinking is smaller for the NWs.

3.2. Electrocatalytic Properties for the Oxygen Reduction Reaction. *Catalyst Activity.* Because the nanowires were free of strongly bound surfactant capping molecules, they were directly used for testing electrocatalysis without any surface treatment. CV and RDE techniques were used to examine the carbon-supported Pt_nAu_{100-n} NWs catalysts for assessing their electrocatalytic ORR in terms of electrochemical active area (ECA), mass activity (MA), and specific activity (SA). The measurements were performed after 30 potential cycles between 0.05 and 1.2 V (vs RHE) in 0.1 M HClO₄ solution saturated with nitrogen at 50 mV/s. Figure 6A shows a typical set of CV curves for PtAu NWs with different compositions. The voltammetric peak characteristics of the alloy NWs in the hydrogen adsorption and desorption region (0–0.4 V) show subtle dependences on the composition, which also exhibit significant differences

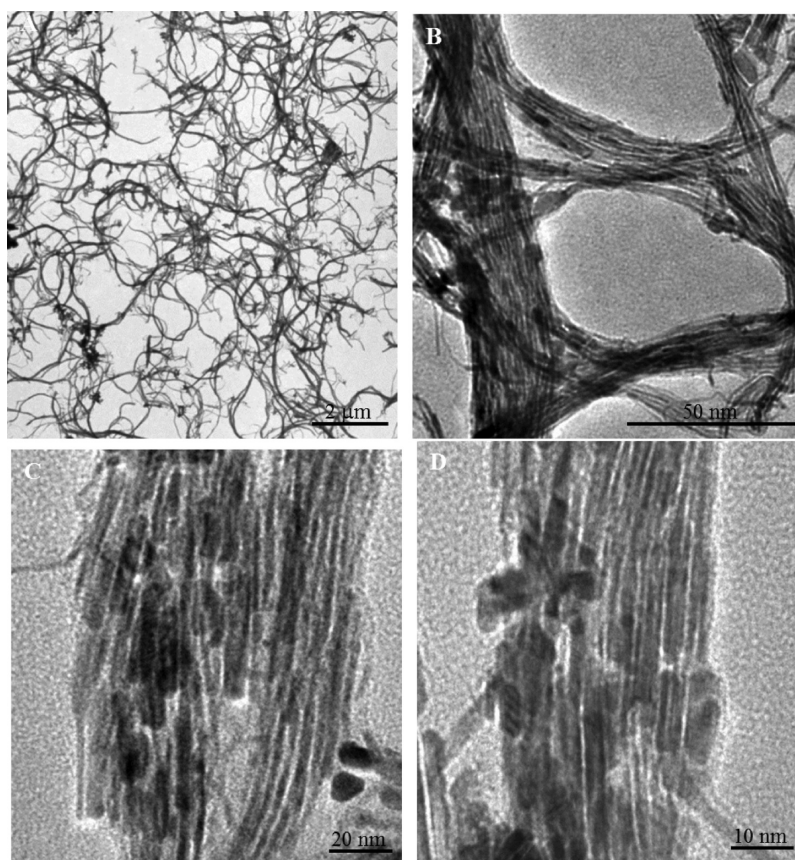


Figure 2. TEM images for Pt₇₂Au₂₈ nanowires (as synthesized) with different magnifications. The average diameter of individual nanowires in the bundles is 4.5 ± 1.0 nm.

in comparison with that for commercial Pt/C catalyst (Figure S7A, SI). The peaks feature a characteristic of (110) facet at 0.12 V and contributions associated with (100)/(111) terraces at 0.24 V.⁵⁹ For PtAu and Pt NWs, the peak associated with (111) or (100)/(111) facet appears to become dominant whereas the peak attributed to (110) is diminished. Note that the voltammetric current in the H_{upd} region for PtAu and Pt NWs features a characteristic flat plateau which is indicative of a relatively large contribution of (111) facets, as shown recently for Pt alloy whisker catalyst.⁶⁰ On the basis of the relative dependence on the composition of the alloy NWs, the (111) peak dominance appears to be most significant for Pt₇₆Au₂₄ NWs. In addition, the overall hydrogen adsorption peaks also show subtle differences for different compositions. In terms of peak currents, Pt₄₉Au₅₁ NWs exhibit the largest peak current whereas Pt₁₆Au₈₄ NWs shows the smallest one. Similar differences are also reflected by comparing the magnitude of the Pt-oxide reduction peaks. As shown in Figure 6B, ECA values of the PtAu NWs, as determined from charges under the hydrogen adsorption waves, exhibit a dependence on the bimetallic composition, revealing a maximum value ($122 \text{ m}^2/\text{g}_{\text{Pt}}$) for $n \sim 49\%$ Pt, which is greater than that for commercial Pt/C ($106 \text{ m}^2/\text{g}_{\text{Pt}}$) (Figure S7B, SI).

Kinetic currents for the ORR were determined by measuring RDE curves in O₂-saturated 0.1 M HClO₄ electrolyte, as shown in Figure 7A for Pt_{*n*}Au_{100-*n*} NWs of different compositions. Because there were differences in Pt loading (i.e., 5.4, 14.0, 10.6, 14.0, and 15.0% for Pt₁₆Au₈₄/C, Pt₄₉Au₅₁/C, Pt₇₆Au₂₄/C, Pt₉₀Au₁₀/C, and Pt/C, respectively), changes in the kinetic currents at 0.900 V (vs RHE) for the catalysts were normalized

against the Pt loading in terms of MA and SA. As shown by mass activity data extracted from the kinetic currents in the RDE curves at 0.900 V in Figure 7A, the mass activity strongly depends on the bimetallic composition, revealing a maximum for Pt₇₆Au₂₄ NWs (Figure 7B). The SA appears to show a trend similar to that of the MA. In this work, we mainly focus on Pt₇₆Au₂₄ NWs for a detailed characterization of NWs' durability and comparison with the NP counterpart. Note that PtAu alloy NWs are found to show an enhanced activity compared with that for Pt NWs. For example, the MA for Pt₇₆Au₂₄ NWs is increased by a factor of 1.9 in comparison with that for Pt NWs, and ~ 2.8 in comparison with commercial Pt ($0.18 \text{ A}/\text{mg}_{\text{Pt}}$) (see Figure S7C, SI).

Durability Test. The stability or durability of the NWs is a critical requirement of catalysts for fuel cell applications, which was assessed by accelerated durability tests of the Pt₇₆Au₂₄/C catalysts in a HClO₄ solution saturated with oxygen gas by repetitive potential cycling between 0.6 and 1.1 V. Figure 8A shows a representative set of CV curves comparing the initial and 10 000th cycles for the Pt₇₆Au₂₄NWs/C catalysts. The ECA is measured by the hydrogen adsorption charges in the H_{upd} region before and after the potential cycling. The charge integrated between 0 and 0.36 V shows a small decrease in ECA, by a factor of $\sim 7\%$, for the Pt₇₆Au₂₄NWs/C catalyst after 10 000th cycles. In Figure 8B, the electrocatalytic activities are compared by comparing the RDE curves. The data reveal a change in the half-wave potential ($E_{1/2}$) after 10 000 cycles by ~ 4 mV. The mass activity extracted from the kinetic current in the RDE data ($0.46 \text{ A}/\text{mg}_{\text{Pt}}$) is shown to decrease only by $\sim 6\%$ in comparison with that before the 10 000 cycles ($0.49 \text{ A}/\text{mg}_{\text{Pt}}$). This result clearly shows that the Pt₇₆Au₂₄ NWs are remarkably durable as a

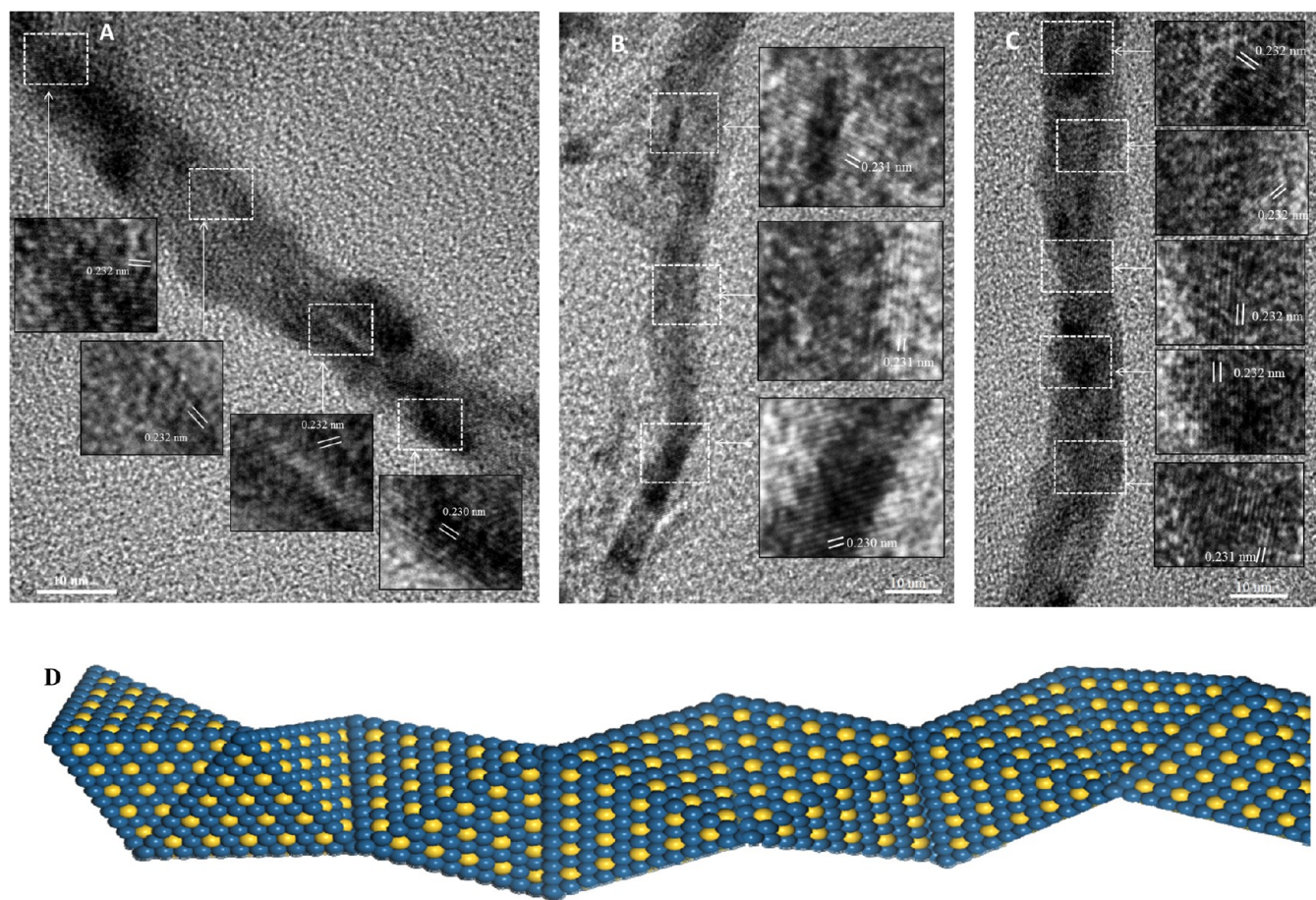


Figure 3. HRTEM images of several samples of $\text{Pt}_{72}\text{Au}_{28}$ nanowires (A, B, and C) where inserts are the magnified views of areas for the determination of the lattice fringes, and a model illustration of the Boerdijk–Coxeter type of helix exhibited by the individual nanowire (D).

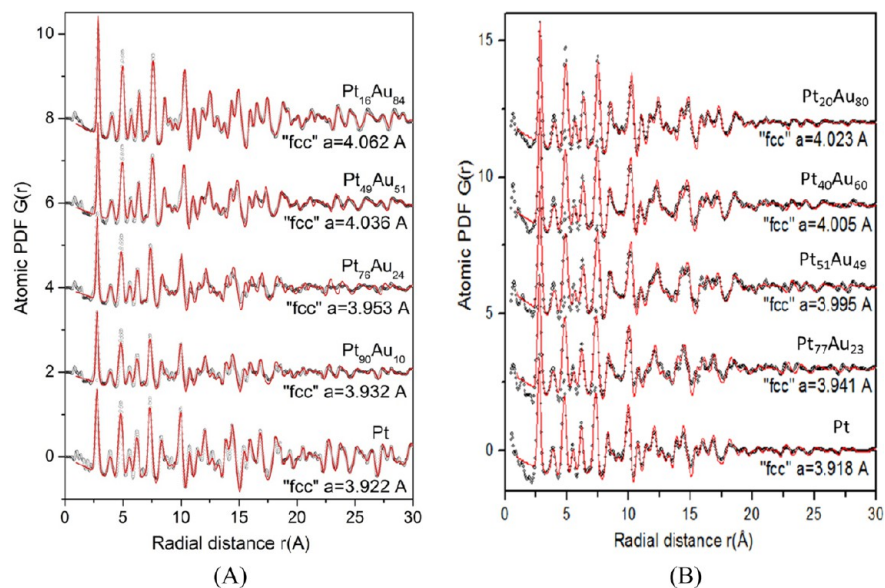


Figure 4. (A) Experimental PDFs (plotted by symbols) and fcc-model fit atomic PDFs (plotted by red lines) for pure Pt and PtAu NWs. (B) Experimental PDFs (plotted by symbols) and model atomic PDFs (plotted as a red line) for 5.1 nm sized Pt and PtAu NPs. The “fcc” lattice parameters refined by the analysis are shown by each set of data.

catalyst for the ORR. A similar result was also obtained for the durability test of the same catalyst in a HClO_4 solution saturated with nitrogen gas by repetitive potential cycling (see Figure S8, SI).

Comparison between NWs and NPs. The electrocatalytic activities of PtAu NWs are also compared with PtAu NPs for the ORR. PtAu NPs of similar compositions were synthesized by the same method for synthesizing the PtAu NWs with a different

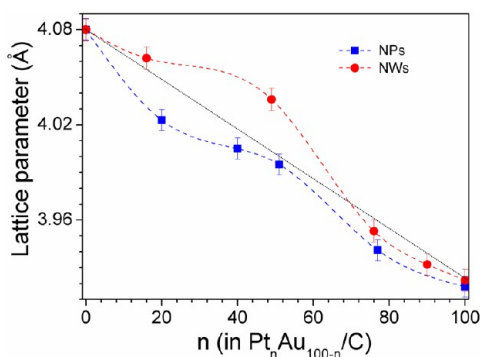


Figure 5. Plots of PDF-fit derived fcc lattice parameters: $\text{Pt}_n\text{Au}_{100-n}$ NWs (red circles) and NPs (blue squares). The dotted red and blue lines provide a general guide to the trend of data points for NWs and NPs. The dotted black line tracks the prediction of Vegard's law based on the lattice parameters of the two metals (Au and Pt).

reaction condition (see [Experimental Section](#)). [Figure 9A](#) shows a representative set of CV curves for $\text{Pt}_{76}\text{Au}_{24}$ NWs/C and $\text{Pt}_{76}\text{Au}_{24}$ NPs/C catalysts in N_2 -purged 0.1 M HClO_4 solutions at room temperature. There are subtle differences for the voltammetric characteristics in the hydrogen adsorption and desorption region (0–0.4 V) and the platinum oxidation and reduction region (0.6–0.8 V). As shown in [Figure 9A](#), $\text{Pt}_{76}\text{Au}_{24}$ NWs exhibit a hydrogen adsorption peak larger than that of the NP counterpart, indicative of a larger ECA value for the NWs.

The electrocatalytic ORR activities are compared by comparing the RDE curves in 0.1 M HClO_4 electrolyte saturated with oxygen for $\text{Pt}_{76}\text{Au}_{24}$ NWs/C and $\text{Pt}_{76}\text{Au}_{24}$ NPs/C catalysts ([Figure 9B](#)). There is a clear difference in the kinetic region of the ORR. The differences are assessed by comparing the mass activity and the specific activity data.

As shown in [Figure 9D](#), $\text{Pt}_{76}\text{Au}_{24}$ NWs exhibit a mass activity of 0.50 $\text{A}/\text{mg}_{\text{Pt}}$. Thus, the value is two times larger than that of the $\text{Pt}_{76}\text{Au}_{24}$ NPs (0.25 $\text{A}/\text{mg}_{\text{Pt}}$). We believe that a greatly increased accessible or effective surface area-to-volume ratio for the nanowires in comparison with nanoparticles is partially operative here. While the theoretical surface area-to-volume ratio for individual nanowires is smaller than that for the nanoparticles, formation of the network structure with open access porosity for the NWs leads to an increased accessibility to the surface or an increased effective surface area. This assessment is supported by a Brunauer, Emmett, and Teller (BET) study of polypyrrole

nanowires and nanoparticles in which the nanowires were shown to exhibit specific surface area higher than that of the nanoparticles by a factor of 15.¹⁹ As evidenced by the experimental data, the ECA for $\text{Pt}_{76}\text{Au}_{24}$ NWs is 3 times larger than that for $\text{Pt}_{76}\text{Au}_{24}$ NPs. Because of the great increase in ECA for $\text{Pt}_{76}\text{Au}_{24}$ NWs which is much more significant than the mass activity, the specific activity of $\text{Pt}_{76}\text{Au}_{24}$ NWs is thus smaller than that of the $\text{Pt}_{76}\text{Au}_{24}$ NPs. The results demonstrate that the NWs, as electrocatalysts for the ORR, are much superior to the NP counterpart in terms of mass activity.

Discussion on Catalytic Synergy. For understanding the observed enhancement of the electrocatalytic ORR over PtAu alloy nanowires, a combination of bifunctional synergy^{35,38} and atomic-scale alloying⁵⁷ was considered in terms of the ensemble effect and ligand effect. In the ensemble effect, there is a dilution of Pt atoms on the surface by Au atoms. For vacuum-deposited Au on Pt (111),⁶¹ scanning tunneling microscopy and cyclic voltammetry measurements revealed that the electrochemical characteristics of the bimetallic surface are dominated by the atomic ratios of Pt and Au at the surface, which is an ensemble effect. The ligand effect involves charge transfer between the two metals or rehybridization of the two metals' orbitals. Theoretical calculation indicates that either direct charge transfer or bond length change constitutes the pathway for electronic perturbation of Pt by Au. In this perturbation, Pt's d band is more filled than that of Au, leading to shift of the d-band center away from the Fermi level. The "d-band model"^{62,63} has been used to explain the trend in the activity enhancement by alloying Pt with transition metals. [Scheme 1A](#) illustrates a proposed catalytic synergy for the ORR over the PtAu alloy NW catalyst featuring predominately (111) facets. The relatively weak binding of the adsorbed oxygen species facilitates their diffusion to adjacent sites on the (111) facet. Direct O_2 reduction to H_2O starts with O_2 adsorption on the surface plane with neighboring atomic sites.⁶⁴ In our experimental observations, a maximum catalytic activity is revealed for a PtAu NW with a Pt: Au ratio close to 76:24, which features predominantly (111) facets as revealed by HE-TEM, and a subtle lattice shrinking as revealed by HE-XRD/PDF analysis. The (111) facet dominance and the Pt–Pt lattice shrinking from the Pt: Au ratio constitutes the basis of the proposed catalytic synergy.

For Pt, the gaining of d electrons would lead to a shift of the d band center away from the Fermi level. This shift weakens the interaction between adsorbed species and the surface Pt atoms. For different Pt: Au ratios, an ensemble effect occurs in which the

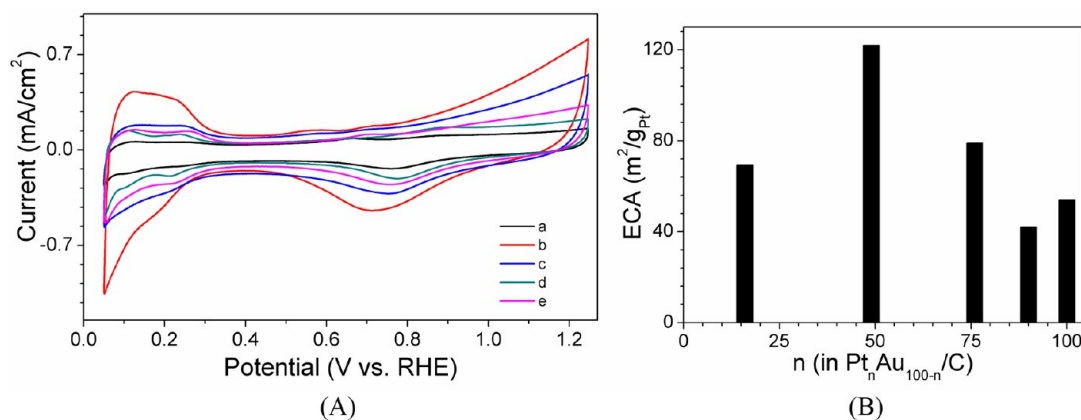


Figure 6. (A) CV curves for $\text{Pt}_n\text{Au}_{100-n}$ NWs of different bimetallic compositions: $\text{Pt}_{16}\text{Au}_{84}/\text{C}$ (a, black), $\text{Pt}_{49}\text{Au}_{51}/\text{C}$ (b, red), $\text{Pt}_{76}\text{Au}_{24}/\text{C}$ (c, blue), $\text{Pt}_{90}\text{Au}_{10}/\text{C}$ (d, green), and Pt/C (e, pink). Glassy carbon electrode (0.196 cm^2) was inked with $10 \mu\text{g}$ of catalyst. Electrolyte was 0.1 M HClO_4 saturated with N_2 (scan rate: 50 mV/s). (B) ECA values vs Pt%.

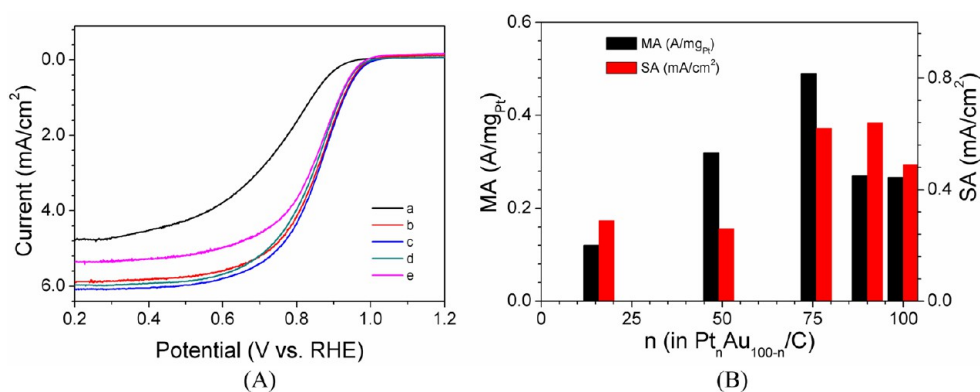


Figure 7. (A) RDE curves for $\text{Pt}_n\text{Au}_{100-n}$ NWs of different compositions: $\text{Pt}_{16}\text{Au}_{84}/\text{C}$ (a, black), $\text{Pt}_{49}\text{Au}_{51}/\text{C}$ (b, red), $\text{Pt}_{76}\text{Au}_{24}/\text{C}$ (c, blue), $\text{Pt}_{90}\text{Au}_{10}/\text{C}$ (d, green), and Pt/C (e, pink). Electrode: Glassy carbon (0.196 cm^2) inked with $10\text{ }\mu\text{g}$ of catalyst. Electrolyte: 0.1 M HClO_4 saturated with oxygen (scan rate: 10 mV/s ; rotation speed: 1600 rpm). (B) Comparison of the MA and SA data at 0.900 V (vs RHE) as a function of Pt% in the PtAu catalyst.

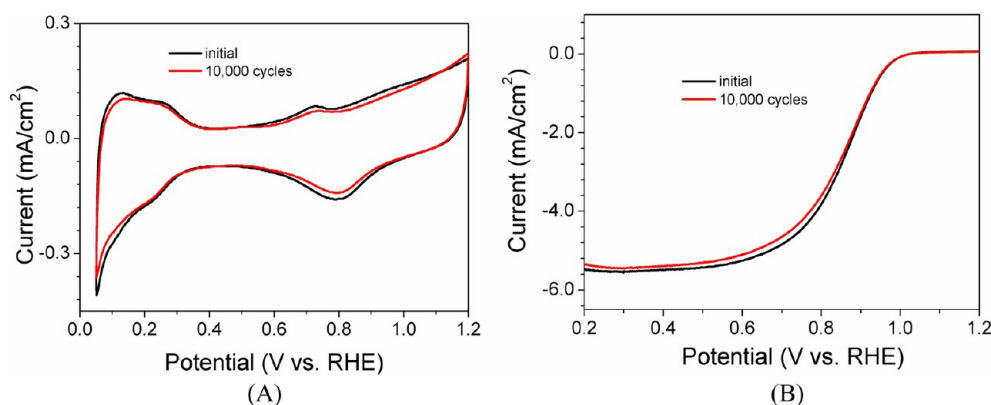


Figure 8. Durability test of the $\text{Pt}_{76}\text{Au}_{24}\text{NWs}/\text{C}$ catalyst for the ORR. (A) CV curves recorded at the beginning of potential cycling and at the end of $10\text{ }000$ cycles (potential scan rate: 50 mV/s ; potential cycle window: 0.6 and 1.1 V) in 0.1 M HClO_4 solution saturated with oxygen. (B) RDE curves for the ORR at the beginning of potential cycling and at the end of $10\text{ }000$ cycles (scan rate: 10 mV/s ; rotation speed: 1600 rpm).

catalytically more active sites (Pt) are diluted by the Au atoms. When the ratio of Pt:Au on the surface is too small, Pt atoms are separated by Au and there are less active sites side by side. When the Pt:Au ratio is too high, Pt cannot gain more d electrons from Au to shift the d band center away from the Fermi level. At an optimum atomic ratio of Pt:Au close to $76:24$ in PtAu alloy, there must be a balance between the Pt and Au surface sites to achieve the optimal electrocatalytic activity and stability, as demonstrated by the significantly improved electrocatalytic activity and stability of PtAu NWs compared with Pt NWs. It is interesting to note that this result agrees with the recent finding based on a 201-atom cluster model ($\text{Pt}_m\text{Au}_{201-m}$), which showed that the d-band center shifts progressively closer to the Fermi energy, at which the density of states is significantly enhanced when the Au content approaches 20%.⁶⁵ For this reason, there must be a unique surface atomic arrangement for 20% Au which produces a maximal charge transfer. In Figure S9, a $\text{Pt}_{151}\text{Au}_{50}$ cluster model is illustrated in terms of the bimetallic distributions in the (111) and (100) facets where the (111) facet is clearly rich in Pt–Pt sites with Au neighboring atoms.

This type of composition-driven optimization of activity is further supported by DFT calculation based on a small PtAu cluster models, yielding binding energy, the d-band center, and cluster geometry (Table S2, SI). The relative stability of the clusters, as reflected by the binding energy, follows the order of $\text{Pt}_2\text{Au}_2 > \text{Pt}_3\text{Au}_1 > \text{Pt}_1\text{Au}_3 > \text{Pt}_4$, indicating that an increase in Pt content would favor the stability enhancement. Molecular

chemisorption of O_2 on the model clusters was also assessed by DFT on the basis of the Yeager model (Scheme 1B, and Table S3, SI). The four-electron transfer in the ORR on Pt mainly occurs through two possible pathways: a direct or parallel pathway, in which the rate-determining step is most likely the first electron transfer to the O_2 species adsorbed on the surface.⁶⁶ The absorption of O_2 by Pt_3Au_1 is stronger than that of other model clusters (Scheme 1B). A stronger Pt–O interaction favors electron transfer and the cleavage of the O–O bond. Moreover, from the partial density of states for d-orbitals in the model clusters (Tables S3, SI), Pt_3Au_1 shows an intermediate value for the d-band center, as compared with the other model configurations, favoring the ORR. On the other hand, the removal of the adsorbed intermediate species (e.g., O and OH) formed after the cleavage of the O–O bond is favored by a weaker adsorption energy for the Pt–O species.⁶⁶ The adsorption energy of the intermediate O species in ORR (E_{O}) on the catalyst surfaces with different catalyst compositions (Table S4, SI) indicates that the adsorption of O on Pt_4 and Pt_1Au_3 are stronger than those on Pt_2Au_2 and Pt_3Au_1 . While the adsorption of O_2 on Pt_3Au_1 is stronger than that on Pt_2Au_2 , the adsorption of O on Pt_2Au_2 (4.72 eV) is much stronger than that on Pt_3Au_1 (4.69 eV). As such, on Pt_2Au_2 there is an indication of tardiness in removing the intermediate O species which hinders the subsequent reaction steps.⁶⁶ The ORR activity for Pt_2Au_2 is thus inferior to that of Pt_3Au_1 owing to the strong O– Pt_2Au_2 interaction. These preliminary results are supportive of a maximum

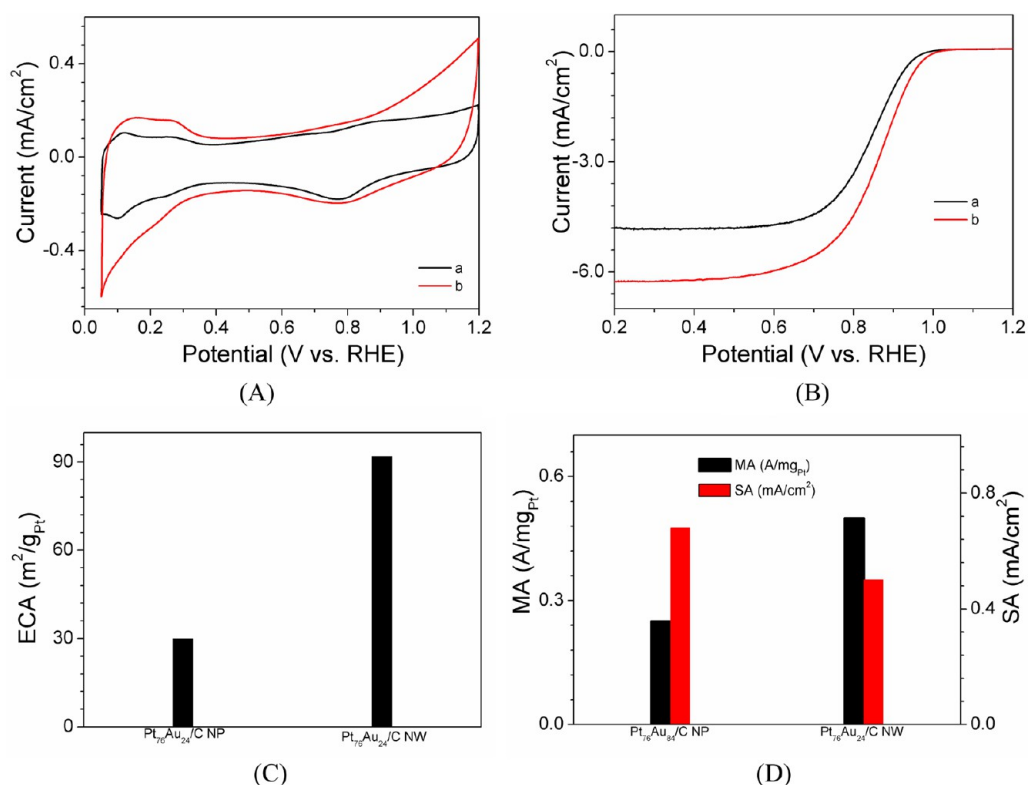
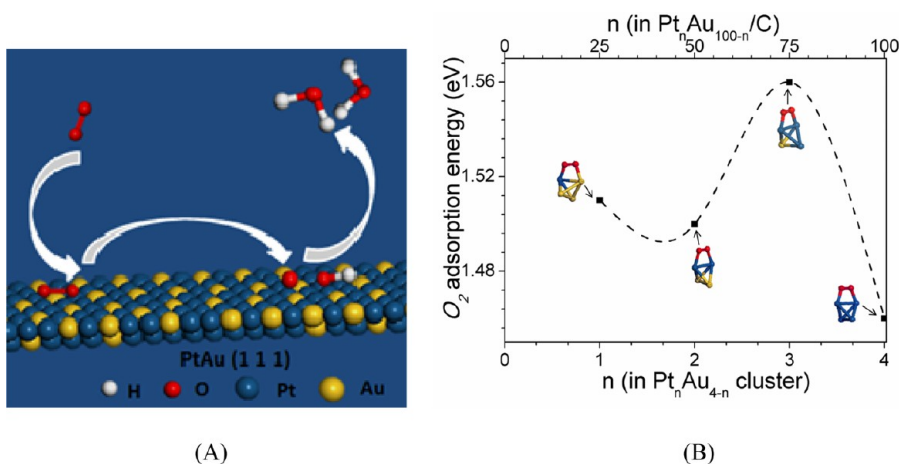


Figure 9. Comparisons between PtAu NWs and NPs. (A) CV and (B) RDE curves for Pt₇₆Au₂₄ NPs/C (a, black) and Pt₇₆Au₂₄ NWs/C (b, red) (electrode: glassy carbon (0.196 cm²) inked with 10 μg of catalyst. Electrolyte: 0.1 M HClO₄ saturated with N₂ for CV and saturated with O₂ for RDE (scan rate: 50 mV/s (CV) and 10 mV/s (RDE); rotation speed: 1600 rpm). (C) ECA values and (D) comparison of the MA and SA data at 0.900 V (vs RHE) for Pt₇₆Au₂₄ NPs/C and Pt₇₆Au₂₄ NWs/C, as a function of Pt% in the PtAu catalyst.

Scheme 1. (A) Catalytic Synergy for Oxygen Reduction Reaction over PtAu NWs Featuring a (111) Facet. (B) Adsorption Energy for Molecular Adsorbed O₂ on Pt_nAu_{4-n} clusters (n = 1–4) Obtained by DFT (see also Tables S2–S4)



ORR activity for Pt₃Au₁, which translates to Pt_nAu_{100-n} with n ~ 75% Pt.

4. CONCLUSION

Ultrathin PtAu alloy nanowires featuring a composition-tunable and parallel-bundled Boerdijk–Coxeter helix type of structure with (111)-dominant facets have been demonstrated for the first time as composition- and facet-tunable catalysts for ORR. The (111) facet dominance and the Pt–Pt lattice shrinking at a Pt:Au ratio of ~3:1, as revealed by HE-TEM and HE-XRD/PDFs analyses of the Pt_nAu_{100-n} NWs with different bimetallic compositions, have been found to play a major role in the

enhancement of the electrocatalytic activity. The ORR activity is shown to exhibit maximum activity at a Pt:Au ratio of ~3:1, the synergy of which is further substantiated by DFT modeling results. In comparison with the catalysts derived from the nanoparticle counterpart with a similar composition and lattice shrinking, the nanowire catalysts were shown to display a higher catalytic activity and stability for ORR. The important role of the (111) facet-dominant surfaces in the catalytic energy of the nanowires is discussed in terms of a combination of bifunctional and the atomic-scale alloying properties, which shines a fresh light on the design and engineering of alloy nanowire catalysts with high catalytic and electrocatalytic activity and durability. Moreover,

in light of recent advances in scale-up hydrothermal synthesis of metal and alloy nanowires,^{49,50,67} there is an encouraging feasibility of scaling up the production of the PtAu NWs described in this work and broadening the applications in other areas of catalysis and electrocatalysis.

■ ASSOCIATED CONTENT

■ Supporting Information

The Supporting Information is available free of charge on the ACS Publications website at DOI: 10.1021/jacs.6b05187.

Figures S1–3, TEM and HR-TEM images for PtAu NWs of different compositions (Pt₁₂Au₈₈, Pt₄₅Au₅₅, and Pt₈₈Au₁₂); Figure S4, TEM image for Pt₇₆Au₂₄ NPs; Figure S5, XRD patterns for PtAu NWs/C catalysts with different bimetallic composition; Figure S6, XRD patterns for Pt₇₆Au₂₄ NWs and NPs; Figure S7, CV curves, ECA, MA, and SA data for NWs in comparison with data of Pt/C; Figure S8, durability test for Pt₇₆Au₂₄/C catalyst; Figure S9, illustration of surface sites for a cuboctahedral Pt₁₅₁Au₅₀ cluster model; Table S2, calculated structure, binding energy, and d-band center for PtAu clusters; Table S3, calculated structure, adsorption energy, and d-band center for molecularly adsorbed oxygen on PtAu clusters; Table S4, adsorption energies of O₂ and intermediate Oads species on PtAu clusters (PDF)

■ AUTHOR INFORMATION

Corresponding Author

*cjzhong@binghamton.edu

Notes

The authors declare no competing financial interest.

■ ACKNOWLEDGMENTS

This work was supported by the Department of Energy – Basic Energy Science Grant (DE-SC0006877), the National Science Foundation (CHE 1566283), and in part the NNSF of China (51271074). The experiments of synchrotron x-ray diffraction were performed at Beamline 11-ID-C of the Advanced Photon Source, a U.S. Department of Energy (DOE) Office of Science User Facility, which is operated for the DOE Office of Science by Argonne National Laboratory under contract no. DE-AC02-06CH11357.

■ REFERENCES

- (1) Sasaki, K.; Naohara, H.; Cai, Y.; Choi, Y. M.; Liu, P.; Vukmirovic, M. B.; Wang, J. X.; Adzic, R. R. *Angew. Chem., Int. Ed.* **2010**, *49*, 8602–8607.
- (2) Avasarala, B.; Murray, T.; Li, W.; Haldar, P. *J. Mater. Chem.* **2009**, *19*, 1803–1805.
- (3) Lu, J. L.; Tang, H. L.; Lu, S. F.; Wu, H. W.; Jiang, S. P. *J. Mater. Chem.* **2011**, *21*, 6668–6676.
- (4) Li, H.; Luk, Y. Y.; Mrksich, M. *Langmuir* **1999**, *15*, 4957–4959.
- (5) Ingram, R. S.; Murray, R. W. *Langmuir* **1998**, *14*, 4115–4121.
- (6) Zhong, C. J.; Luo, J.; Njoki, P. N.; Mott, D.; Wanjala, B. N.; Loukrakpam, R.; Lim, S.; Wang, L. Y.; Fang, B.; Xu, Z. C. *Energy Environ. Sci.* **2008**, *1*, 454–466.
- (7) Zhong, C. J.; Luo, J.; Fang, B.; Wanjala, B. N.; Njoki, P. N.; Loukrakpam, R.; Yin, J. *Nanotechnology* **2010**, *21*, 062001.
- (8) Shukla, A. K.; Raman, R. K. *Annu. Rev. Mater. Res.* **2003**, *33*, 155–168.
- (9) Adler, S. B. *Chem. Rev.* **2004**, *104*, 4791–4843.

- (10) Loukrakpam, R.; Luo, J.; He, T.; Chen, Y. S.; Xu, Z. C.; Njoki, P. N.; Wanjala, B. N.; Fang, B.; Mott, D.; Yin, J.; Klar, J.; Powell, B.; Zhong, C. J. *J. Phys. Chem. C* **2011**, *115*, 1682–1694.
- (11) Loukrakpam, R.; Shan, S. Y.; Petkov, V.; Yang, L. F.; Luo, J.; Zhong, C. J. *J. Phys. Chem. C* **2013**, *117*, 20715–20721.
- (12) Luo, J.; Maye, M. M.; Petkov, V.; Kariuki, N. N.; Wang, L. Y.; Njoki, P.; Mott, D.; Lin, Y.; Zhong, C. J. *Chem. Mater.* **2005**, *17*, 3086–3091.
- (13) Wanjala, B. N.; Luo, J.; Loukrakpam, R.; Fang, B.; Mott, D.; Njoki, P. N.; Engelhard, M.; Naslund, H. R.; Wu, J. K.; Wang, L. C.; Malis, O.; Zhong, C. J. *Chem. Mater.* **2010**, *22*, 4282–4294.
- (14) Xia, Y. N.; Yang, P. D.; Sun, Y. G.; Wu, Y. Y.; Mayers, B.; Gates, G.; Yin, Y. D.; Kim, F.; Yan, H. Q. *Adv. Mater.* **2003**, *15*, 353–389.
- (15) Koenigsmann, C.; Wong, S. S. *Energy Environ. Sci.* **2011**, *4*, 1161–1176.
- (16) Li, B.; Yan, Z. Y.; Higgins, D. C.; Yang, D. J.; Chen, Z. W.; Ma, J. X. *J. Power Sources* **2014**, *262*, 488–493.
- (17) Sun, S. H.; Zhang, G. X.; Geng, D. S.; Chen, Y. G.; Li, R. Y.; Cai, M.; Sun, X. L. *Angew. Chem., Int. Ed.* **2011**, *50*, 422–426.
- (18) Zhang, J. L.; Vukmirovic, M. B.; Xu, Y.; Mavrikakis, M.; Adzic, R. R. *Angew. Chem., Int. Ed.* **2005**, *44*, 2132–2135.
- (19) Rawal, I.; Kaur, A. *Sens. Actuators, A* **2013**, *203*, 92–102.
- (20) Koenigsmann, C.; Santulli, A. C.; Gong, K. P.; Vukmirovic, M. B.; Zhou, W. P.; Sutter, E.; Wong, S. S.; Adzic, R. R. *J. Am. Chem. Soc.* **2011**, *133*, 9783–9795.
- (21) Koenigsmann, C.; Zhou, W. P.; Adzic, R. R.; Sutter, E.; Wong, S. S. *Nano Lett.* **2010**, *10*, 2806–2811.
- (22) Koenigsmann, C.; Sutter, E.; Chiesa, T. A.; Adzic, R. R.; Wong, S. S. *Nano Lett.* **2012**, *12*, 2013–2020.
- (23) Chen, B.; Cheng, D. J.; Zhu, J. Q. *J. Power Sources* **2014**, *267*, 380–387.
- (24) Wang, X.; Figueroa-Cosme, L.; Yang, X.; Luo, M.; Liu, J. Y.; Xie, Z. X.; Xia, Y. N. *Nano Lett.* **2016**, *16*, 1467–1471.
- (25) Zhang, L.; Roling, L. T.; Wang, X.; Vara, M.; Chi, M. F.; Liu, J. Y.; Choi, S.; Park, J.; Herron, J. A.; Xie, Z. X.; Mavrikakis, M.; Xia, Y. N. *Science* **2015**, *349*, 412–416.
- (26) Valden, M.; Lai, X.; Goodman, D. W. *Science* **1998**, *28*, 1647–1650.
- (27) Chen, M. S.; Kumar, D.; Yi, C. W.; Goodman, D. W. *Science* **2005**, *310*, 291–293.
- (28) Kim, Y. D.; Fischer, M.; Ganteför, G. *Chem. Phys. Lett.* **2003**, *377*, 170–176.
- (29) Xu, Y.; Mavrikakis, M. *J. Phys. Chem. B* **2003**, *107*, 9298–9307.
- (30) Zhang, J.; Sasaki, K.; Sutter, E.; Adzic, R. R. *Science* **2007**, *315*, 220–222.
- (31) Van Brussel, M.; Kokkinidis, G.; Vandendael, I.; Buess-Herman, C. *Electrochem. Commun.* **2002**, *4*, 808–813.
- (32) El-Deab, M. S.; Ohsaka, T. *Electrochim. Acta* **2002**, *47*, 4255–4261.
- (33) Fang, B.; Wanjala, B. N.; Hu, X.; Last, J.; Loukrakpam, R.; Yin, J.; Luo, J.; Zhong, C. J. *J. Power Sources* **2011**, *196*, 659–665.
- (34) Luo, J.; Njoki, P. N.; Lin, Y.; Wang, L.; Zhong, C. J. *Electrochem. Commun.* **2006**, *8*, 581–587.
- (35) Luo, J.; Njoki, P. N.; Lin, Y.; Mott, D.; Wang, L.; Zhong, C. J. *Langmuir* **2006**, *22*, 2892–2898.
- (36) Malis, O.; Radu, M.; Mott, D.; Wanjala, B.; Luo, J.; Zhong, C. J. *Nanotechnology* **2009**, *20*, 245708.
- (37) Wanjala, B. N.; Luo, J.; Fang, B.; Mott, D.; Zhong, C. J. *J. Mater. Chem.* **2011**, *21*, 4012–4020.
- (38) Mott, D.; Luo, J.; Njoki, P. N.; Lin, Y.; Wang, L. Y.; Zhong, C. J. *Catal. Today* **2007**, *122*, 378–385.
- (39) Yang, S. C.; Hong, F.; Wang, L. Q.; Guo, S. W.; Song, X. P.; Ding, B. J.; Yang, Z. M. *J. Phys. Chem. C* **2010**, *114*, 203–207.
- (40) Teng, X. W.; Han, W. Q.; Wang, Q.; Li, L.; Frenkel, A. I.; Yang, J. C. *J. Phys. Chem. C* **2008**, *112*, 14696–14701.
- (41) Cherevko, S.; Xing, X. L.; Chung, C. H. *Electrochim. Acta* **2011**, *56*, 5771–5775.
- (42) Yi, X. J.; Yu, G.; Chang, F. F.; Xie, Z. H.; Tran, T. N.; Hu, B. N.; Zhong, C. J. *Chem. - Asian J.* **2014**, *9*, 2612–2620.

- (43) Han, X. Y.; Wang, D. W.; Liu, D.; Huang, J. S.; You, T. Y. *J. Colloid Interface Sci.* **2012**, *367*, 342–347.
- (44) Tian, X. X.; Li, J. J.; Xu, D. S. *Electrochem. Commun.* **2010**, *12*, 1081–1083.
- (45) Song, P.; Li, S. S.; He, L. L.; Feng, J. J.; Wu, L.; Zhong, S. X.; Wang, A. J. *RSC Adv.* **2015**, *5*, 87061–87068.
- (46) Zhou, Y. B.; Yu, G.; Chang, F. F.; Hu, B. N.; Zhong, C. J. *Anal. Chim. Acta* **2012**, *757*, 56–62.
- (47) Xiao, M. L.; Li, S. T.; Zhu, J. B.; Li, K.; Liu, C. P.; Xing, W. *ChemPlusChem* **2014**, *79*, 1123–1128.
- (48) Tan, Y. M.; Fan, J. M.; Chen, G. X.; Zheng, N. F.; Xie, Q. J. *Chem. Commun.* **2011**, *47*, 11624–11626.
- (49) Xia, B. Y.; Wu, H. B.; Yan, Y.; Lou, X. W.; Wang, X. J. *Am. Chem. Soc.* **2013**, *135*, 9480–9485.
- (50) Lu, W. B.; Ge, J.; Tao, L.; Cao, X. W.; Dong, J.; Qian, W. P. *Electrochim. Acta* **2014**, *130*, 335–343.
- (51) Shan, S. Y.; Petkov, V.; Yang, L. F.; Luo, J.; Joseph, P.; Mayzel, D.; Prasai, B.; Wang, L. Y.; Engelhard, M.; Zhong, C. J. *J. Am. Chem. Soc.* **2014**, *136*, 7140–7151.
- (52) Xia, M. R.; Ding, W.; Xiong, K.; Li, L.; Qi, X. Q.; Chen, S. G.; Hu, B. S.; Wei, Z. D. *J. Phys. Chem. C* **2013**, *117*, 10581–10588.
- (53) Wang, L.; Wang, Y.; Song, S. Q.; Shen, P. K. *Chin. J. Catal.* **2009**, *30*, 433–439.
- (54) Wang, L. C.; Williams, J. I.; Lin, T.; Zhong, C. J. *Catal. Today* **2011**, *165*, 150–159.
- (55) Zhu, Y. H.; He, J. T.; Shang, C.; Miao, X. H.; Huang, J. F.; Liu, Z. P.; Chen, H. Y.; Han, Y. *J. Am. Chem. Soc.* **2014**, *136*, 12746–12752.
- (56) Velázquez-Salazar, J. J.; Esparza, R.; Mejía-Rosales, S. J.; Estrada-Salas, R.; Ponce, A.; Deepak, F. L.; Castro-Guerrero, C.; José-Yacamán, M. *ACS Nano* **2011**, *5* (8), 6272–6278.
- (57) Mendoza-Cruz, R.; Bazán-Díaz, L.; Velázquez-Salazar, J. J.; Plascencia-Villa, G.; Bahena-Urbe, D.; Reyes-Gasga, J.; Romeu, D.; Guisbiers, G.; Herrera-Becerra, R.; José-Yacamán, M. *Nano Lett.* **2016**, *16*, 1568–1573.
- (58) Petkov, V.; Wanjala, B. N.; Loukrakpam, R.; Luo, J.; Yang, L. F.; Zhong, C. J.; Shastri, S. *Nano Lett.* **2012**, *12*, 4289–4299.
- (59) Devivaraprasad, R.; Ramesh, R.; Naresh, N.; Kar, T.; Singh, R. K.; Neergat, M. *Langmuir* **2014**, *30*, 8995–9006.
- (60) van der Vliet, D. F.; Wang, C.; Tripkovic, D.; Strmcnik, D.; Zhang, X. F.; Debe, M. K.; Atanasoski, R. T.; Markovic, N. M.; Stamenkovic, V. *R. Nat. Mater.* **2012**, *11*, 1051–1058.
- (61) Bergbreiter, A.; Alves, O. B.; Hoster, H. E.; Waldman, T.; Reichert, R.; Koper, M. T. M. *ChemPhysChem* **2010**, *11*, 1505–1512.
- (62) Nørskov, J.; Rossmeisl, J.; Logadottir, A.; Lindqvist, L.; Kitchin, J. R.; Bligaard, T.; Jonsson, H. *J. Phys. Chem. B* **2004**, *108*, 17886–17892.
- (63) Kitchin, J. R.; Nørskov, J. K.; Barteau, M. A.; Chen, J. G. *J. Chem. Phys.* **2004**, *120*, 10240–10246.
- (64) Greeley, J.; Nørskov, J. K.; Mavrikakis, M. *Annu. Rev. Phys. Chem.* **2002**, *53*, 319–348.
- (65) Mikkath, J. H.; Schwingschlögl, U. *J. Mater. Chem. A* **2013**, *1*, 9885–9888.
- (66) Shao, M. H.; Liu, P.; Zhang, J. L.; Adzic, R. J. *J. Phys. Chem. B* **2007**, *111*, 6772–6775.
- (67) Li, Z. C.; Gu, A. J.; Guan, M. Y.; Zhou, Q. F.; Shang, T. M. *Colloid Polym. Sci.* **2010**, *288*, 1185–1191.